Three-Dimensional Si/Ge Quantum Dot Crystals

13 AUTHORS, INCLUDING:

Elisabeth Müller
Paul Scherrer Institut
176 PUBLICATIONS **3,354** CITATIONS

SEE PROFILE

Yasin Ekinci
Paul Scherrer Institut
100 PUBLICATIONS **1,564** CITATIONS

SEE PROFILE

R.T. Lechner
Montanuniversität Leoben
52 PUBLICATIONS **1,368** CITATIONS

SEE PROFILE

Stefan Birner
nextnano GmbH
52 PUBLICATIONS **762** CITATIONS

SEE PROFILE

Three-Dimensional Si/Ge Quantum Dot Crystals

Detlev Grützmacher,*,†,‡ Thomas Fromherz,§ Christian Dais,‡ Julian Stangl,§
Elisabeth Müller,‡ Yasin Ekinci,‡ Harun H. Solak,‡ Hans Sigg,‡ Rainer T. Lechner,§
Eugen Wintersberger,§ Stefan Birner,‖ Václav Holý,⊥ and Günther Bauer§

*Institute of Bio- and Nanosystems 1, Semiconductor Nanoelectronics,
Forschungszentrum Jülich, D-52425 Jülich, Germany, Laboratory for Micro- and
Nanotechnology, Paul Scherrer Institut, CH-5232 Villigen-PSI, Switzerland,
Institut für Halbleiter und Festkörperphysik, Johannes Kepler University Linz,
Altenbergerstr. 69, A-4040 Linz, Austria, Walter Schottky Institut, Technical University
Munich, Am Coulombwall 3, D-85748 Garching, Germany, and nextnano³,
Frauenmantelanger 21, D-80937 Munich, Germany, and Department of Condensed
Matter Physics, Masaryk University, Kotlářská 2, 611 37 Brno, Czech Republic*

ABSTRACT

Modern nanotechnology offers routes to create new artificial materials, widening the functionality of devices in physics, chemistry, and biology. Templated self-organization has been recognized as a possible route to achieve exact positioning of quantum dots to create quantum dot arrays, molecules, and crystals. Here we employ extreme ultraviolet interference lithography (EUV-IL) at a wavelength of $\lambda = 13.5$ nm for fast, large-area exposure of templates with perfect periodicity. Si(001) substrates have been patterned with two-dimensional hole arrays using EUV-IL and reactive ion etching. On these substrates, three-dimensionally ordered SiGe quantum dot crystals with the so far smallest quantum dot sizes and periods both in lateral and vertical directions have been grown by molecular beam epitaxy. X-ray diffractometry from a sample volume corresponding to about 3.6×10^7 dots and atomic force microscopy (AFM) reveal an up to now unmatched structural perfection of the quantum dot crystal and a narrow quantum dot size distribution. Intense interband photoluminescence has been observed up to room temperature, indicating a low defect density in the three-dimensional (3D) SiGe quantum dot crystals. Using the Ge concentration and dot shapes determined by X-ray and AFM measurements as input parameters for 3D band structure calculations, an excellent quantitative agreement between measured and calculated PL energies is obtained. The calculations show that the band structure of the 3D ordered quantum dot crystal is significantly modified by the artificial periodicity. A calculation of the variation of the eigenenergies based on the statistical variation in the dot dimensions as determined experimentally ($\pm 10\%$ in linear dimensions) shows that the calculated electronic coupling between neighboring dots is not destroyed due to the quantum dot size variations. Thus, not only from a structural point of view but also with respect to the band structure, the 3D ordered quantum dots can be regarded as artificial crystal.

A quantum dot, sometimes also called an artificial atom, can be built up by semiconductor nanostructures either by defining a potential well in a two-dimensional (2D) carrier gas[1] via gate contacts on the sample surface or by using the self-assembly of dots via the Stranski−Krastanow growth mode.[2] The first method allows only 2D arrays of quantum dots and appears technologically very demanding if large, densely packed quantum dot arrays are aimed at. The second method, the growth of self-assembled quantum dots performed on planar substrates leads to random nucleation of dots with a rather broad size distribution. To circumvent these

inherent problems of random nucleation, templated self-assembly of semiconductor nanostructures has attracted considerable attention lately.[3−5] This technology combines the advantages of conventional top-down lithographic techniques with bottom-up approaches like self-organization. So far, most of the work was carried out on InAs/GaAs dots,[6−8] although some studies on the ordering of Ge islands on Si substrates have also been performed.[3,4,9−11] Technologically, the Si/Ge system is of great interest because the fabrication processes for integrated Si-based circuits are well controlled for critical dimensions down to a few 10 nm so that the realization of spintronics[12,13] and even quantum computation[14] based on these processes can be envisioned. However, we would like to emphasize that Ge dots fabricated in a Si matrix form a type II band alignment, thus the Ge dots themselves form a potential well only for holes, whereas the electrons

* Corresponding author. E-mail: d.gruetzmacher@fz-juelich.de.
† Forschungszentrum Jülich.
‡ Paul Scherrer Institut.
§ Johannes Kepler University Linz.
‖ Technical University Munich and nextnano³.
⊥ Masaryk University.

are confined in the vicinity of the Ge dots, i.e., by the tensile and compressive strain fields in the Si matrix induced by the QDs.[15] Besides their potential for electronic and optical applications, SiGe alloys are used as thermoelectric materials. For PbSe−PbTe quantum dot superlattices, it has been shown that three-dimensional (3D) ordering of the quantum dots (QDs) dramatically enhances the thermoelectric figure of merit as compared to random alloys due to increased phonon scattering reducing thermal conductivity.[16] Similar effects can be expected in the Si/SiGe system.

Here the fabrication of ordered Ge dots in 2D and 3D arrays, providing structures suitable for vertical and lateral coupling of Ge dots, have been studied. The formation of 2D and 3D quantum dot crystals demands the nucleation of dots at predefined sites on the substrates. Previous reports, using mesa lines,[17] dislocation networks,[18] or ripple structures induced by growth instabilities during the Si buffer layer deposition,[19] permit an improvement in the ordering of Ge dots compared to the growth on blanket Si wafers, however, the ordering is not perfect enough to fabricate a "quantum dot crystal", i.e., an array of quantum dots that is periodic in three dimensions forming a lattice of quantum dots in a host crystal. Lithographic techniques are required for the fabrication of templates with sufficient perfection in periodicity and size of the predefined dot nucleation sites. Electron-beam (e-beam) lithography,[7,9] ion-beam lithography,[5,11] and optical interference lithography[20] have been performed to fabricate prepatterns on Si substrates. Whereas the first two approaches write the pattern for the nucleation site for each individual dot sequentially, the optical interference technique allows the prepatterning of large areas with 2D arrays in a single exposure. For e-beam and ion-beam lithography, the determination of the location of each nucleation site is limited by the resolution of the instrument, which is approximately 5 nm, thus interdot distances may vary by few nanometers. Device architectures relying on tunneling processes between dots may not tolerate such an amount of variations in the tunnel barrier width. With conventional optical interference lithography, it is only possible to achieve periodicities of the pattern down to $\lambda/2$, thus using a wavelength λ of about 200 nm periodicities larger than 100 nm are accessible. In general, the 2D Ge dot arrays reported so far have considerably larger interdot distances, thus lateral coupling between dots will be too weak.[7,21]

Extreme ultraviolet interference lithography at a wavelength of $\lambda = 13.5$ nm allows an excellent precision, and pattern control in the subnanometer regime has been achieved using EUV instead of optical beams.[22,23] Moreover, the method allows for the formation of patterns with less than 30 nm periodicity. We want to point out that small imperfections of the mask do not affect the periodicity of the interference pattern used for exposure. Thus EUV-IL is suitable for producing templates for the growth of densely packed, electronically lateral coupled Ge dot arrays. Whereas previous studies have been valuable to understand the fundamental nucleation properties of islands on patterned surfaces, EUV-IL offers a realistic path for the formation of artificial crystals both in an electronic and structural sense. The impact of exposure dose, etching, and deposition parameters on the 2D ordering phenomena of Ge dots has been studied previously.[24]

In this study, we report the formation of nearly perfect 3D QD ordering with the so far smallest QD sizes and periods both in lateral and vertical directions and a detailed statistical analysis based on X-ray diffraction and AFM experiments. EUV-IL has been employed for the prepatterning of Si(100) substrates,[23,24] which have been used as the starting material for the deposition of 3D quantum dot crystals. The details of the 2D pattern fabrication using EUV-IL have been previously reported.[24] In our experiments, an interference mask with four gratings resulting in the exposure of a square lattice was used. In principle, also more complicated arrangements like hexagonal lattices can be achieved by using six or more gratings. While the EUV-IL setup allows for the illumination of a field of 2×2 mm² in a single exposure, in our experiments, typically fields of 700×700 μm² were exposed. Subsequent to EUV-IL exposure, the photoresist is developed and the pattern is transferred into the Si by reactive ion etching (RIE). A very shallow pattern of only 8−10 nm depth is produced by RIE on the Si surface. A typical pattern used in this study has a periodicity of 90 nm by 100 nm following the suggestion of Friesen et al.[25] for the design of Si-based quantum dot qubits. Next, the PMMA is stripped and contaminants are removed. A 50 nm thick Si buffer layer is deposited at 300 °C by molecular beam epitaxy (MBE) without further high-temperature annealing of the sample before deposition. The buffer layer growth leads to a transformation of the squarelike depressions etched into the Si surface into narrow inverted tiplike holes of 3−4 nm depth. The deposition of seven monolayers (ML) of pure Ge at 450 °C leads to the formation of {105}-faceted islands on the surface[24] as investigated by AFM. The islands form only in the pits on the Si surface, resulting in an extremely uniform array of Ge dots. The Ge dots in the first layer fill the pits prepared by EUV-IL and RIE due to capillary forces.[26] Histograms of the size distribution reveal for the Ge dots in this first layer a diameter of 45 ± 3.2 nm and a height of 4.2 ± 0.37 nm, i.e., less than 9% variation. For comparison, on a sample area without pattern, the dots nucleate randomly and exhibit a broad bimodal size distribution, with dot diameters and heights ranging from 10 to 80 nm and 1 to 10 nm, respectively. Thus the growth of Ge dots on the prepatterned surface not only led to close to perfectly regimented arrays of dots but also to a dramatic improvement of the size distribution.

The subsequent island layers are grown by depositing five ML of Ge on top of the planar Si spacer layer, hence the islands are smaller than those in the first layer. In addition, Figure 1a and its inset show that, due to the filling of the pits, the QDs in the first layer have a higher aspect ratio than the ones in the subsequent layers, although both types of dots have {105} top facets. All Ge dot layers were overgrown with about 10 nm Si at low temperatures, ramped from 300 to 450 °C during the deposition to reduce intermixing of the Ge dots with the Si cap layer, which
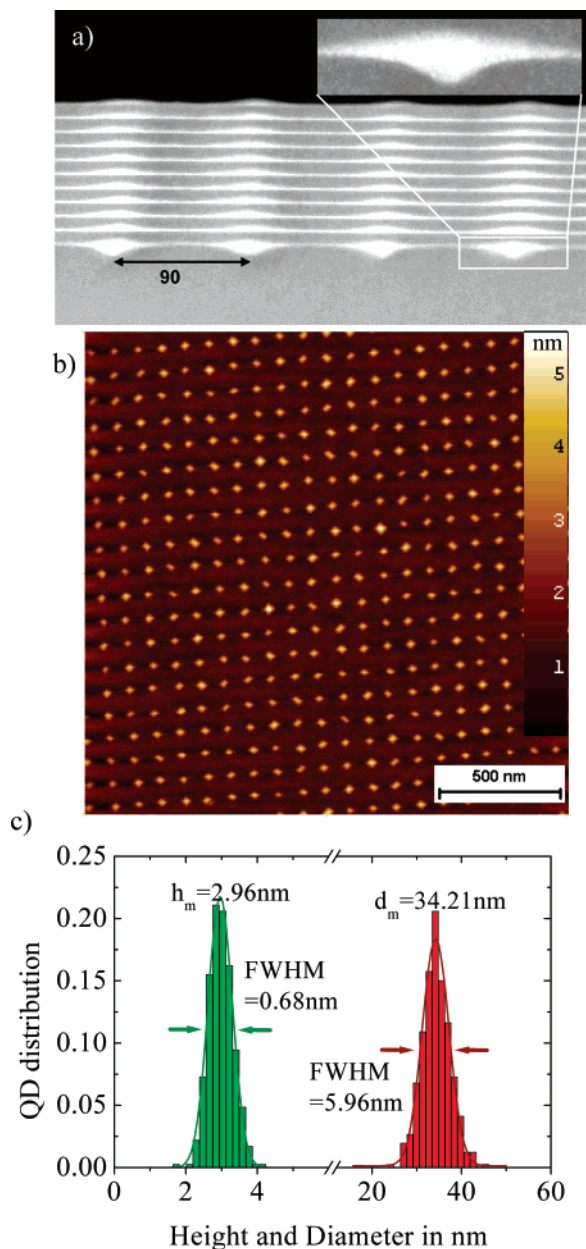
Figure 1. Images of 10 period stacks of Ge islands and Si spacer layer (10 nm) deposited on a prepatterned area. Panels (a) and (b) show cross-sectional TEM micrographs and AFM data, respectively). The inset in (a) shows a closeup of a dot in the first layer. The comparison of the cross-sectional TEM micrographs and the AFM images demonstrates that the vertical and the lateral ordering is maintained after 10 periods on the prepatterned substrate. For dots grown on the prepatterned area, the corresponding histogram (panel c) illustrates the narrow size distribution in diameter and height of the Ge dots at the top surface of the 3D quantum dot crystal.

provides a flat surface for the subsequent Ge dot growth. In the five ML Ge layers, the dots nucleate on top of the buried ones due to the strain fields created by them.[27] This self-alignment of the dots in subsequent layers can be used to build up three-dimensional quantum dot crystals with high lateral and vertical perfection. Figure 1a shows a TEM of a cross-sectional view of a 3D quantum dot crystal containing a stack of 10 QD layers grown on top of the first layer in that the dots have nucleated at the predefined positions. The

lateral periodicity is 90 nm × 100 nm and the vertical periodicity is close to 11 nm. The AFM surface scan shown in Figure 1b depicts the surface after the deposition of 10 island layers. The islands on the top are {105} faceted and have a square base. The AFM scan indicates that the lateral periodicity is well preserved and no missing or extra dots can be found in the AFM of the topmost Ge layer, even when the scan range is increased to 8 μm × 8 μm. The size distribution is shown in Figure 1c. The height of these small hut clusters is 2.96 ± 0.34 nm and their diameter is 34.21 ± 2.98 nm, i.e., the variations are comparable to those in the first layer. For comparison, TEM and AFM investigations were performed also for the QD stack deposited on a nonpatterned area of the same sample. The bimodal size distribution of dots in the first layer containing hut and dome clusters leads to a strongly disordered dot arrangement in the course of the stacking of dot layers. The dome clusters with their steeper side facets, i.e., larger height compared to the hut clusters, lead to strong strain fields and preferred nucleation sites for islands in the successive layers. Thus the dome clusters increase in size up to the size of superdomes[28] at the expense of the hut clusters.

To obtain more detailed information on the structural perfection of the Ge quantum dot crystals, X-ray diffraction was employed at the ID10B (Troika II) beam line at the European Synchrotron Radiation Facility, Grenoble, France. Reciprocal space maps in the [110] azimuth were recorded around the symmetrical (004) and the asymmetrical (224) Bragg peaks. As an example, the scattered X-ray intensity distribution for a (224) reciprocal space map is shown in Figure 2 in which Q_x and Q_z denote reciprocal space coordinates along orthogonal [110] and [001] directions. Using an incident beam size of 100 × 200 μm², only the prepatterned area was illuminated. The regular arrangement of islands leads to a series of satellite maxima both in growth direction as well as in lateral direction. In between the vertical satellite maxima, fringes due to the total thickness of the SiGe dot stack are visible even for higher lateral satellite order, indicating the high perfection of the 3D dot crystal. For the lateral and vertical periods, we obtain values of 100.2 and 11.46 nm, respectively. By changing the azimuth by 90°, an in-plane period of 90.7 nm is found. Thus the measurements reflect accurately the design value of a 90 nm by 100 nm array. The large number of satellites resolved indicates crystalline perfection of the quantum dot crystal, which is unmatched so far for X-ray analysis of any semiconductor quantum dot system. The number of resolved satellite peaks may not be even limited by the perfection of the dot crystal but rather by the fact that the pattern is not aligned perfectly with the crystalline direction of the Si substrate, consequently, the intensity maxima drift out of the scattering plane with increasing order, distorting the envelopes. By mapping around the (224) reciprocal lattice point, it becomes clear that the envelope of the satellites is shifted to small Q_x values, which is an indication of elastic relaxation in the Ge islands.

To determine the mean chemical composition of the Ge dots from the (004) and (224) reciprocal space maps, a detailed comparison of measured and simulated reciprocal
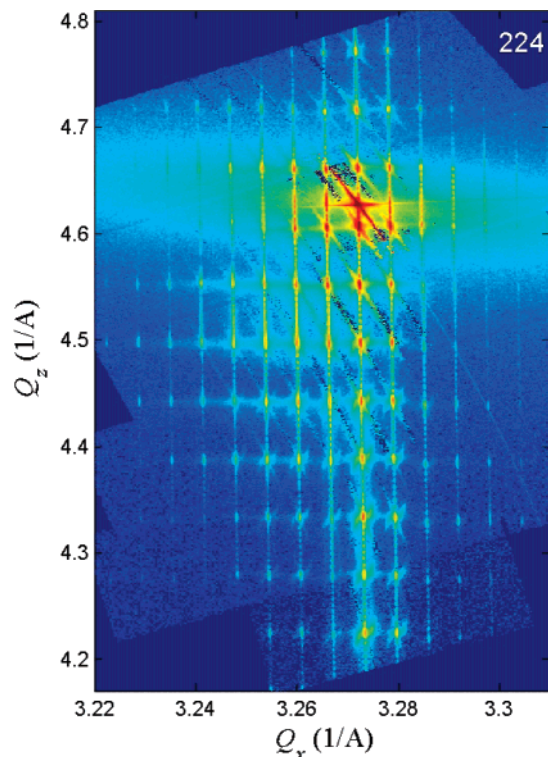
Figure 2. Reciprocal space maps around (224) Bragg peaks taken from a three-dimensional Si−Ge quantum dot crystal with 10 periods.

Figure 3. Temperature-dependent (10−300 K) photoluminescence of a Si−Ge quantum dot crystal containing a seed layer grown on a prepatterned substrate and subsequently 10 periods of dots.

space maps was performed. For the simulation of the diffracted intensities, the strain fields were obtained by analytical calculations using the Fourier method.[29] The corresponding displacement fields $u(r)$ served as an input for the calculated intensities based on a kinematical approximation. The integrated intensities of the satellites of the (004) and (224) reciprocal space maps were simulated because these are almost independent from any disorder and the best match was obtained for $x_{Ge} = 0.60$. From the reciprocal space maps, it is also possible to determine a quantitative parameter describing a disorder of the lateral dot positions. If the dots were ideally laterally arranged in the whole volume of the quantum dot crystal, the scattered intensity would be concentrated in intensity maxima, corresponding to the points of the lattice reciprocal to the 3D dot lattice. A lateral disorder in the dot positions gives rise to lateral intensity sheets in reciprocal space, the shapes of which along the Q_x axis depend on the probability distribution of the displacement of the dots from their ideal positions. The intensity sheets are visible in the measured intensity maps (see Figure 2). To determine the root mean square displacement σ of the dots from their ideal positions, we have extracted vertical linear scans parallel to the Q_z axis between the coherent intensity satellites from the reciprocal space maps. From the intensity maxima in these scans, we have reconstructed the Q_x dependence of the intensity of the diffuse sheets. We have fitted this dependence to the theoretical long-range order model of the positional disorder,[30] and we obtained the value of $\sigma = a \times (0.12 \pm 0.05)$ nm, where a denotes the lateral dot period. Analysis of the AFM images shows that, locally, the perfection of the dot
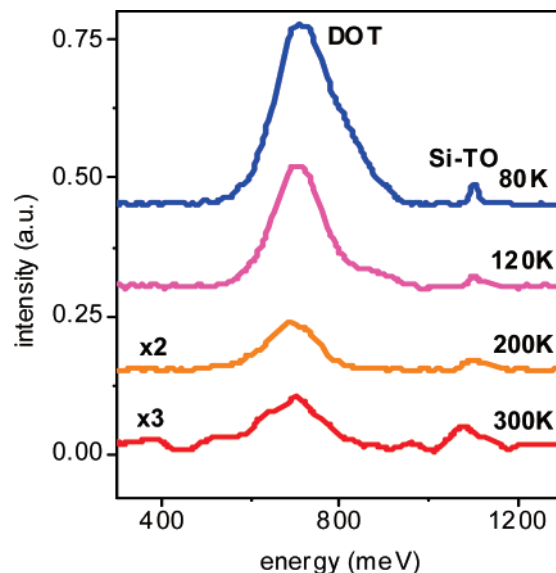
lattice is even better, however, the X-ray data represent the statistical average over about 0.15×0.2 mm², i.e., 3.6×10^7 dots.

Figure 3 shows temperature-dependent photoluminescence (PL) spectra obtained from this 3D quantum dot crystal. The topmost dot layer is exposed to air and hence does not contribute to the measured PL intensity. At low temperatures, the spectrum reveals a strong line centered at 746 meV. This line shifts to higher energies while increasing the temperature. The luminescence persists up to room temperature. The narrow PL line associated with the TO-phonon resonance of the Si substrate is found at 1090 meV and gradually vanishes with an increase in temperature.

To interpret the PL spectra correctly, one has to consider that the radiative transitions in this Si/Ge system are both indirect in real and in reciprocal space. Thus the complexity of the confinement situation for electrons and holes in these structures has to be taken into account. This has been done based on the simulation package nextnano³.[31] Within nextnano³, in a first step, the strain fields in the QDs and the Si matrix were calculated by minimizing the elastic energy. Using the structural data obtained from the X-ray and AFM measurements, the resulting strain fields are in excellent agreement with those calculated analytically for the simulation of the X-ray results. The strain fields were used to calculate the strain-induced spatial variation and splitting of the conduction- and valence-band edges by linear deformation potential theory. The deformation potential constants used in the calculations are collected from literature data.[32] The band offset between the average of the Si and $Si_{1-x}Ge_x$ valence bands for unstrained bulk crystals ($\Delta E_{av} = E_{av}^{SiGe} - E_{av}^{Si}$) was calculated according to $\Delta E_{av} = 580 \times x$ meV.[32] The unstrained band gap of a SiGe alloy was calculated according to Weber et al.[33] Using these equations, the total variation of the conduction and valence bands as well as their splitting due to the strain can be calculated
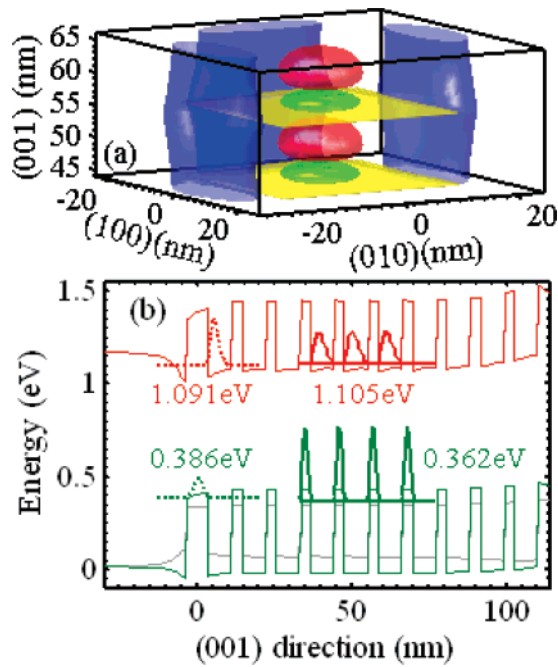
Figure 4. (a) Illustration of isosurfaces for electron and hole wave functions within the two $Si_{0.4}Ge_{0.6}$ dots in the center of an 11-fold stack. A detailed description is found in the text. (b) Calculation of the alignment for the Δ_z (red thin lines), HH (green thin lines), and LH (gray thin lines) energy bands in stacked Si−Ge quantum dots along the axis through the quantum dot centers. The squared moduli of the Δ_z and HH wavefunctions along the $(0,0,z)$ line in panel (a) are shown by the red and green bold lines, respectively. For each wavefunction plot, the origin of the ordinate axis was aligned with the eigenenergy of the respective states. The degenerate states in the center of the QD column are shown by the full lines, whereas the Δ_z and HH ground states in the QD column are shown by the broken lines. The numbers given in the plot indicate the energies of the respective states, where zero energy corresponds to the average of the heavy hole, light hole and split-off valence band energies in unstrained Si.

everywhere in the QD crystal. In these potential landscapes, for each band a single-particle, single-band, effective-mass Schrödinger equation is solved to calculate eigenenergies and carrier distribution probabilities by the nextnano[3] simulation package.

For the structural parameters obtained by X-ray analysis and AFM measurements, the band structure for the 10-layer QD stack on top of the seeding layer was calculated. In Figure 4a, the calculated charge distribution around the two QDs in the center of the 10-layer stack is shown. In this figure, the interface between the QDs (modeled as a pyramid in agreement with the cross-sectional TEM picture shown in Figure 1) and the Si matrix is shown in yellow. The green, red, and blue surfaces confine those regions, in that $|\psi_i(\mathbf{r})|^2\rangle$ $0.1 \times \max(|\psi_i(\mathbf{r})|^2)$, where $\psi_{i=HH,\Delta z,\Delta xy}(\mathbf{r})$ denote the ground-state wave functions for the heavy holes (HH, green), electrons in the Δ valleys parallel (Δ_z, red) and perpendicular (Δ_{xy}, blue) to the growth direction (the Δ_{xy} state in the positive (100) direction is omitted for better visibility). While the HH are confined to the Ge-rich interior of the QDs, the electrons are localized in the Si matrix adjacent to the QD. We want to point out that the electron confinement is purely due to the strain in the Si matrix, which is tensile above the

apex and below the base of the QD and compressive around the base of the QD. The strain causes a splitting of the originally degenerated Si conduction band minima in Δ direction. Thus, depending on the sign of the strain, the Δ_z or Δ_{xy} states have locally the lowest electron energies, resulting in a spatial separation of the Δ_z or Δ_{xy} ground-state wave function shown in Figure 4a. For the QD states in the center of the QD stack shown in Figure 4a, the eigenenergies $E_{HH} = 362$ meV, $E_{\Delta xy} = 1158$ meV, and $E_{\Delta z} = 1105$ meV are calculated (the origin of the energy scale is set to the average of the three valence bands in unstrained Si).

In Figure 4b, the band edge profiles for the Δ_z (red line), HH (green line), and light holes (LH, gray line) along the growth direction through the center of a QD column (i.e., along the $(0,0,z)$ line in Figure 4a) are shown by the thin lines, together with the squared moduli of the Δ_z (red) and HH (green) ground states (broken lines) and the energetically lowest Δ_z (red) and highest HH states (green) localized in the center of the QD stack (bold, full lines). The difference of the lowest electron energy ($E_{\Delta z}$) and the largest hole energy (E_{HH}) $E_{\Delta z} - E_{HH} = 743$ meV calculated for the states localized in the center of the QD stack excellently agrees with the measured peak position in the PL spectrum of this sample, indicating that structural parameters as obtained by X-ray are highly reliable.

Figure 4b shows that the band edge profiles are not periodic along the growth direction. This is due to the fact that, to achieve vertical ordering, the period of the QD stack along the growth direction has to be chosen smaller than the decay length of the strain fields. Thus the strain accumulates or decays along the growth direction depending on the strength and spatial distribution of strain sources within a distance on the order of one strain decay length. For the QD stacks discussed in this work, Figure 4b shows that the strain originating from the larger QDs in the first layer is still significantly influencing the band edge profiles in the second layer, and the free sample surface modifies the band edge profile already in layer nine. In the center of the QD stack from layers three to nine, subsequent layers have virtually the same band structure (64% of all QDs) and determine the PL peak position. Slightly stronger strain-induced variations of the bandedges along the QD stack growth direction were reported in refs 34 and 35 for islands with higher Ge concentration. Thus, the variation of the strain fields along the growth direction of stacked dots leads to a variation of the PL transition energies of stacked Ge dots, and an inhomogeneously broadened line width would be observed even if the Ge dots would be all perfectly the same. In our quantum dot crystals, the Ge islands have a size distribution of around ±10%, which leads to an additional broadening of the PL line. Considering the fact that at the large excitation density usually used in these PL experiments, electron−hole pairs are excited in Ge dots throughout the dot crystal, the observed rather large width of the PL peak of the QD crystal shown in Figure 3 can be understood in spite of the uniformity of the QD crystal as indicated by the X-ray diffraction. The PL spectrum of the sample does not

show resolved wetting layer luminescence, consistent with literature data,[35] where this effect has been explained by tunneling between closely spaced island layers.

Figure 4a shows that for the QD dimensions of the samples investigated in this work, the electron states of subsequent dot layers are coupled. This is most evident for the Δ_{xy} states (shown in blue in Figure 4a) that are completely delocalized parallel to the growth direction and form a 1D miniband in the artificial QD crystal, but also the Δ_z states bound in the potential minima above the apex and below the base of subsequent QD layers are strongly coupled. However, in the results of the simulations, no indication for coupling of the Δ_z states through the quantum dots, resulting in miniband formation as recently reported in ref 36, was found.

To estimate the impact of size variations on the details of the band structure, calculations varying the height and diameter of the dots have been performed. For the Δ_z and Δ_{xy} states, a change in volume of the dot by 1% leads to variations of 0.3 and 0.1 meV, respectively. Considering 10% variation in the linear dimensions (i.e., ~30% volume variation), which is slightly larger than indicated by the AFM and TEM data, the electronic states will shift by 9 and 3 meV, respectively. For the Δ_{xy} states, the 3 meV energy variation is smaller than the miniband width and thus will not hamper miniband formation, nor will the 9 meV energy variation decouple the Δ_z states bound in the potential minima above the apex and below the base of subsequent QD layers.

Further reducing the lateral period will result in the lateral coupling of the two Δ_{xy} minibands belonging to adjacent dot stacks. Moreover, the nextnano[3] simulations show that, for QD stacks laterally separated less than approximately 5 nm, their compressive strain fields strongly overlap, resulting in a reduction of the Δ_{xy} band edges. Further increasing the confinement energy of the Δ_z state by a reduction of the vertical period eventually will shift the Δ_z energy above the Δ_{xy} energy. In this situation, the delocalized Δ_{xy} artificial crystal states become the electron ground states, and a significant modification of the transport and optical properties of the artificial QD crystal can be expected. Aiming at arrangements with a 30 nm period and dot diameters of 25 nm (i.e., a lateral dot separation of about 5 nm) appears to be well within the capability of EUV-IL.

The complex structure of the electron confinement depends strongly on the shape of the dots, as shown in Figures 4a,b. Because the confinement and possible tuning of the coupling of the wave functions in applications like quantum computing[37] strongly depends on the ability to localize and couple electronic states, it appears to be required to gather detailed knowledge about the shape and the composition of the islands. Using X-ray diffraction on assemblies of dots with a narrow size distribution in combination with energy-resolved high-resolution TEM and scanning probe microscopy might be a possible path to collect these insights. The lateral and vertical coupling of SiGe dots in dense arrays may provide also new specific properties of phonon spectra, as suggested in ref 38.

In conclusion, this work demonstrates the feasibility of a technology for the fabrication of ordered quantum dot structures. In particular, 3D quantum dot crystals with extraordinary structural perfection of the quantum dot lattice have been demonstrated using templated self-organization. Moreover, this technology bears the potential to create quantum dots at addressable positions that can be precisely located with respect to existing device layers on the substrate. The templates were fabricated using EUV interference lithography, which proved to be ideal for patterning nano-structures into Si substrates with high accuracy. The quantum dot crystals deposited by MBE on these templates were found to be of excellent crystalline perfection and exhibit low defect densities, thus suitable for a comprehensive analysis comparing structural and optical data with model calculations. The material is well suited for further studies to implement quantum dot structures in nanoelectronics, spintronics, and possibly future structures for quantum computing as well as for optoelectronic devices based on Si.

References

(1) Laux, S. E.; Frank, D. J.; Stern, F. *Surf. Sci.* **1988**, *196*, 101.
(2) Leonhard, D.; Krishnamurthy, M.; Reaves, C. M.; Denbaars, S. P.; Petroff, P. M. *Appl. Phys. Lett* **1993**, *63*, 3203; Apetz, R.; Vescan, L.; Hartmann, A.; Loo, R.; Dieker, C.; Carius, R.; Lüth, H. *Mater. Sci. Technol.* **1995**, *11*, 425.
(3) Kiravittaya, S.; Rastelli, A.; Schmidt, O. G. *Appl. Phys. Lett.* **2005**, *87*, 243112.
(4) Zhong, Z.; Halilovic, A.; Fromherz, T.; Schäffler, F.; Bauer, G. *Appl. Phys. Lett.* **2003**, *82*, 4779.
(5) Gray, J. L.; Atha, S.; Hull, R.; Floro, J. A. *Nano Lett.* **2004**, *4*, 2447.
(6) Lee, H.; Johnson, J. A.; Speck, J. S.; Petroff, P. M. *J. Vac. Sci. Technol., B* **2000**, *18*, 2193.
(7) Baier, M. H.; Watanabe, S.; Pelucchi, E.; Kapon, E. *Appl. Phys. Lett.* **2004**, *84*, 1943.
(8) Kiravittaya, S.; Rastelli, A.; Schmidt, O. G. *Appl. Phys. Lett.* **2006**, *88*, 043112.
(9) Schmidt, O. G.; Eberl, K. *IEEE Trans. Electron Devices* **2001**, *48*, 1175.
(10) Schmidt, O. G. Jin-Phillipp, N. Y.; Lange, C.; Denker, U.; Eberl, K.; Schreiner, R.; Grabeldinger, H.; Schweizer, H. *Appl. Phys. Lett.* **2000**, *77*, 4139.
(11) Karmous, A.; Cuenat, A.; Ronda, A.; Berbezier, I.; Atha, S.; Hull, R. *Appl. Phys. Lett.* **2004**, *85*, 6401.
(12) Vrijen, R.; Yablonovitch, E.; Wang, K.; Jiang, H. W.; Balandin, A.; Roychowdhury, V.; Mor, T.; DiVincenzo, D. *Phys. Rev. A* **2000**, *62*, 012306.
(13) Malissa, H.; Jantsch, W.; Mühlberger, M.; Schäffler, F.; Wilamowski, Z.; Draxler, M.; Bauer, P. *Appl. Phys. Lett.* **2004**, 85, 1739. Tyryshkin, A. M.; Lyon, S. A.; Jantsch, W.; Schäffler, F. *Phys. Rev. Lett.* **2005**, *94*, 126802.
(14) Wang, K. L. *J. Nanosci. Nanotechnol.* **2002**, *2*, 235.
(15) Fukatsu, S.; Sunamura, H.; Shiraki, Y.; Komiyama, S. *Appl. Phys. Lett.* **1997**, *71*, 258.
(16) Majumdar, A. *Science* **2004**, *303*, 777 and references cited therein.
(17) Kamins, T. I.; Williams, R. S.; Basile, D. P. *Nanotechnology* **1999**, *10*, 117.
(18) Leroy, F.; Eymery, J.; Gentile, P.; Fournel, F. *Appl. Phys. Lett.* **2002**, *80*, 3078−3080.

(19) Lichtenberger, H.; Mühlberger, M.; Schäffler, F. *Appl. Phys. Lett.* **2005**, *86*, 131919.

(20) Zhong, Z.; Bauer, G. *Appl. Phys. Lett.* **2004**, *84*, 1922.

(21) Zhong, Z.; Chen, G.; Stangl, J.; Fromherz, T.; Schäffler, F.; Bauer, G. *Physica E* **2004**, *21*, 588.

(22) Solak, H. H.; David, C.; Gobrecht, J.; Golovkina, V.; Cerrina, F.; Kim, K. O. Nealey, P. F. *Microelectron. Eng.* **2003**, *67−68*, 56.

(23) Solak, H. H. *Microelectron. Eng.* **2005**, *78−79*, 410.

(24) Dais, Ch.; Solak, H. H.; Ekincis, Y.; Müller, E.; Sigg, H.; Grütz-macher, D. *Surf. Sci.* **2007**, *601*, 2787.

(25) Friesen, M.; Rugheimer, P.; Savage, D. E.; Lagally, M. G. van der Weide, D. W.; Joynt, R.; Eriksson, M. A. *Phys. Rev. B* **2003**, *67*, 121301.

(26) Biasiol, G.; Gustafsson, A.; Leifer, K.; Kapon, E. *Phys. Rev. B* **2002**, *65*, 205306.

(27) Tersoff, J.; Teichert, C.; Lagally, M. G. *Phys. Rev. Lett.* **1996**, *76*, 1675.

(28) Kamins, T. I.; Medeiros-Ribeiro, G.; Ohlberg, D. A. A.; Williams, R. S. *J. Appl. Phys.* **1999**, *85*, 1159.

(29) Stangl, J.; Holý, V.; Bauer, G. *Rev. Mod. Phys.* **2004**, *74*, 725.

(30) Wollschläger J.; Larsson, M. *Phys. Rev. B* **1998**, *57*, 14937.

(31) For a review on nextnano³, see: Majewski, J. A.; Birner, S.; Trellakis, A.; Sabathil, M.; Vogl, P. *Phys. Status Solidi C* **2004**, *1*, 2003.

(32) van de Walle, C. G. In *Properties of Silcon Germanium and SiGe*: *Carbon*; Kasper, E., Lyutovich, K., Eds.; Emis Datareviews Series 24; INSPEC: London, 2000, Vol. 135−143, pp 149−157.

(33) Weber, J.; Alonso, M. I. *Phys. Rev. B* **1989**, *40*, 5683.

(34) Schmidt, O. G.; Eberl, K.; Rau, Y. *Phys. Rev. B* **2000**, *62*, 16715.

(35) Schmidt, O. G.; Eberl, K. *Phys. Rev. B* **2000**, *61*, 13721.

(36) Talalaev, V. G.; Cirlin, G. E.; Tonkikh, A. A.; Zakharov, N. D.; Werner, P.; Gösele, U.; Tomm, J. W.; T. Elsaesser, *Nanoscale Res. Lett.* **2006**, *1*, 137.

(37) Loss, D.; DiVincenzo, D. P. *Phys. Rev. A* **1998**, *57*, 120.

(38) Lazarenkova, O. L.; Balandin, A. A. *Phys. Rev. B* **2002**, *66*, 245319.

NL0717199